 DOI: 10.1086/699869

Appendix from G. Kletetschka et al., "Cosmic-Impact Event in Lake Sediments from Central Europe Postdates the Laacher See Eruption and Marks Onset of the Younger Dryas" (J. Geol., vol. 126, no. 6, p. 000)

Introduction

A sediment sequence for studying the onset of the YD episode in central Europe was collected from Stara Jimka lake (SJ), which was earlier identified to contain sediment of suitable age (Mentlík et al. 2010). This paleolake has an area of up to 6.5 ha and a maximum depth of sediment deposits of 10 m. It is situated at an altitude 1110 m in a northwest-oriented catchment of size 148 ha with a maximum altitude of 1314 m. Assuming today's 1300 mm/y of precipitation (Kliment et al. 2011), the paleolake would have had an annual average outflow of ~40 L/s and ~40 d of residence time. The paleolake had well-developed soil and vegetation cover in the catchment from the Allerød period, a littoral zone with emergent and submerged vegetation, and both planktonic and benthic communities.

The cores from the SJ site provide a stratigraphic record of climate change typical for central Europe from the postglacial period through the Holocene (Heiri et al. 2014). This includes relative climatic warmth between 14,700 and 12,900 cal BP (the Bølling-Allerød interstadial), followed by YD cooling and then a return to warmth during the Holocene. Tephra layers represent important synchronization markers in sedimentary archives, and therefore we looked for any tephra indication in SJ sediment.

We collected several overlapping core sections from the same site. We geochemically correlated the suite of cores by using Rb variations determined with XRF scans for each core at a resolution of 2 mm (fig. A1). We determined that the core-matching procedure allows for the relative depth uncertainty of 1 cm (table 3).

Methods

Field Activities

A total of eight 50-cm-long cores were removed from seven drill holes (separated from each other by no more than 5 m) at the SJ site with a Russian peat sampler (chamber corer) from the surface down to 5 m. We also collected 10 additional 1-m-long cores in plastic sleeves from two nearby locations with a pneumatic corer. This material was used for nonmagnetic separation of MSPs, while all of the other analyses were conducted on the samples collected by the chamber corer.

The chamber corer was inserted into the soil in a closed position down to the desired sampling level and then twisted so that sample from the desired depth was trapped in the chamber. The probe contains a chamber that is a 50-cm-long half-cylinder with a radius of 3.5 cm. Material filling the chamber (fig. 1*B*) was retrieved separately from a depth between 3 and 5 m. These provided a stratigraphic record extending back to the end of last glacial period at ~14,000 cal BP (Mentlík et al. 2010).

XRF Scans

To obtain core XRF scans, we built a programmable, horizontally moving platform. The main structure was constructed of wood, while the mechanical parts were mostly of steel. We used a NEMA 23 stepper motor with torque of 1.89 Nm, firmly attached to the main structure. The torque is transferred by a lead screw and nut to allow horizontal movement of the core platform. The platform is connected to the moving screw with a hardened linear shaft. For the hardware driver we used HY-DIV168N-3.5, which was made for a two-phase hybrid stepper motor using a Toshiba 6560 chip. The stepper and driver are powered by a 220-V industrial power supply. The device connects to a personal computer via USB with an Arduino UNO microcontroller and computer. We wrote a C++ script for programming the movement of the platform via the Arduino controller. The XRF analyzer software is controlled in parallel with the Arduino microcontroller via a macro loop using one computer in real time.

Each core was placed in the sediment holder and covered with a polyethylene membrane (thickness of 9 μm), and its surface was adjusted with a planar glass plate for flatness. We used Geochem mode with two beams (the first beam up to 11 keV for lighter elements for 10 min and a second beam up to 50 keV for heavier elements for 10 min). We performed XRF analyses along the flattened core samples in 2-mm steps, using a 2.2-mm collimated beam, with 20 min of exposure at each core location. An XRF analyzer (Delta Professional, 50-KeV X-ray with 2.2-mm collimated beam size) was tagged to the core position, and this allowed us to assign all of the retrieved cores to a common depth on the basis of variations in Rb concentration (fig. A1).

Pollen and Charcoal

Pollen and charcoal were extracted from core SJD 2, which was sampled at a depth resolution of 1 cm without gaps between samples. Samples were digested in potassium hydroxide (KOH). One cubic centimeter of the sample was placed in a test tube, and 10 mL of 10% KOH was added. Then the samples were placed in a boiling water bath for 10–15 min and stirred with a glass rod to break up the material. The samples were next passed through a fine plastic sieve with a mesh size of 120 μm, which allowed all pollen and spores to pass through but retained larger particulate matter, such as sand grains and plant fragments. Then the tubes were balanced with distilled water and centrifuged for 3 min at 2900 rpm with a swing-out head centrifuge. This resulted in deposition of a small pellet of material (sediment). Next, the pellet was suspended in distilled water with a glass stirring rod. The samples were placed in plastic bottles and submerged in HF for 48 h, and then the samples were dehydrated. After this, the samples were suspended in glacial acetic acid, which dehydrates the organic material. After centrifuging and decanting, we added about 6 mL of acetolysis mixture to the sediment and resuspended it by stirring with a glass rod. That mixture consisted of acetic anhydride mixed with fresh concentrated sulfuric acid in a ratio of 9:1 by volume. Then the samples were centrifuged, decanted, resuspended in glacial acetic acid, centrifuged, and decanted. The last steps were to resuspend the pellet in distilled water, centrifuge, and decant the supernatant. The washing process was repeated to remove all residual acetic acid. The pollen samples were mounted in glycerin, ready for examination by light microscopy.

For charred organic-material quantification, a total of 46 samples were processed, corresponding to core levels 427.4–473.1 cm. Charcoal particles were counted under a reflected-light microscope (50–500 ×) on the basis of black opaque color and angular edges. Other macroremains occurring in the sediment also were counted, including *Isoëtes* sp. megaspores, *Chara* sp. oogonia, and cladoceran ephippia.

MSP Extraction

Core SJF 3 contained the BV and MSP layers. The MSPs we found are morphologically and geochemically similar to those collected in North America, Central America, Belgium, and Germany. We cut the core segments into 2-mm slices, and for each slice we measured magnetic susceptibility and performed the standard separation technique to isolate MSPs (Israde-Alcántara et al. 2012). For nonmagnetic separation, we used material obtained by pneumatic corer. We utilized heavy liquids to obtain high-density material from the layer containing MSPs within the several cores extracted by pneumatic corer. The depth containing MSPs was previously identified with 50-cm cores SJF 3 and SJF 4, where MSPs were found approximately 2–3 cm above the BV (fig. 1*B*). We separated a 2-cm-tall cylinder of sediment, whose base was located 2 cm above the BV in the core material extracted by pneumatic corer. Grains from this sediment were separated with sieves of various sizes (100, 200, 325, 400 mesh size, corresponding to 37, 44, 74, and 149 μm, respectively). The separated material was then cleaned of excess clay via ultrasound, and the separates were analyzed under an optical microscope. Suspected objects were manually placed on glass plates with nonmagnetic tools. The spherules' level of magnetism was measured with a 2G superconducting rock magnetometer. Their natural remanent magnetization was first demagnetized. Then the spherules were magnetized with a 1-T pulse magnetizer, and this magnetization was demagnetized (see "LMR Analysis" below). Finally, the spherules were identified with a scanning electron microscope (SEM).

Chironomids and Cladocerans

The rest of the core material was dried and used for collection and counting of microfossils, with a focus on chironomids and cladocerans. Altogether, nine selected samples were analyzed between core depths 442.4 and 452.4 cm in core

SJF 3. Subsequent sample preparation for chironomid analysis (Brooks et al. 2007) used warm 1% KOH and Euparal slide mounts. The remains of the chironomid head capsules were rinsed with distilled water through a 100-μm sieve and handpicked from a Sedgewick-Rafter counting cell with fine steel needles and a dissecting microscope (30–40 × magnification). The head capsules were identified under a compound microscope (200 × and 400 × magnification) with the standard procedure (Wiederholm 1983; Brooks et al. 2007). Similarly, chitinous remains of Cladocera (head shields, shells, postabdomens, postabdominal claws, and ephippia) were extracted in warm 1% KOH, rinsed with distilled water through a 40-μm sieve, colored, and identified under a compound microscope (200 × and 600 × magnification).

Chronology

Four dates were obtained from the bulk SJ sediment. One date each was obtained from cores SJF 4 (413.2 cm) and SJI I (448.5 cm), and two samples for dating were collected from core SJD 2 (450.4 and 459.2 cm). Beta Analytic (Miami) performed the ^{14}C dating according to standard protocols. In order to determine the age of the MSP-rich layer, we used Bayesian statistical analysis (OxCal, ver. 4.2.4) and the radiocarbon ages (table 2) to develop an age-depth model (Bronk Ramsey 2009).

Chemical Analyses

Other than XRF, chemical analyses were performed on homogenized samples from sediments at the YDB layer (447.9–448.9 cm), below this layer (449.5–450.5 cm), and above it (445.7–446.7 cm) with ICP-MS measurements at Charles University. Organic content in the sediment samples (~1 g of dry sediment per sample) was measured by the LOI method via oven drying (105°C, 18 h) and muffle furnace heating (550°C, 4 h).

SEM

We used a modern automated mineralogical approach that has been adopted for detailed analyses of the tephra distribution within a sedimentation profile (Gottlieb et al. 2000; US Patent 20,130,054,153). The TESCAN integrated mineral analyzer (TIMA) housed at the Institute of Geology at the Czech Academy of Sciences was used for the automated search and identification of tephra fragments. The data were collected with the newly introduced "dot mapping" mode. For "dot mapping," a back-scattered electron (BSE) image is taken first (0.3-μm "pixel spacing" in our case). Individual particles, as well as preliminary phases/segments, are determined only with the BSE image. Then a suitable place inside each preliminary phase/segment is chosen, and each phase is covered by a rectangular mesh (0.9-μm "dot spacing" in our case) of measurement points, with a chosen point taken as the origin of the mesh. Then X-ray spectra are acquired at each measurement point (if the particle is smaller than the mesh, only an analysis at the origin/center of the particle is performed). The combination of the high-resolution BSE image and the lower-resolution spectroscopic data is used to improve the phase segmentation when the spectroscopic data show that a preliminary phase/segment comprises multiple mineral phases with different chemistries. A 1-mm-wide and 50-mm-long section through a sedimentation profile was scanned with more than 549 million data points, used to create 12 million EDS analyses to provide the base for localization and distribution analysis of tephra fragments.

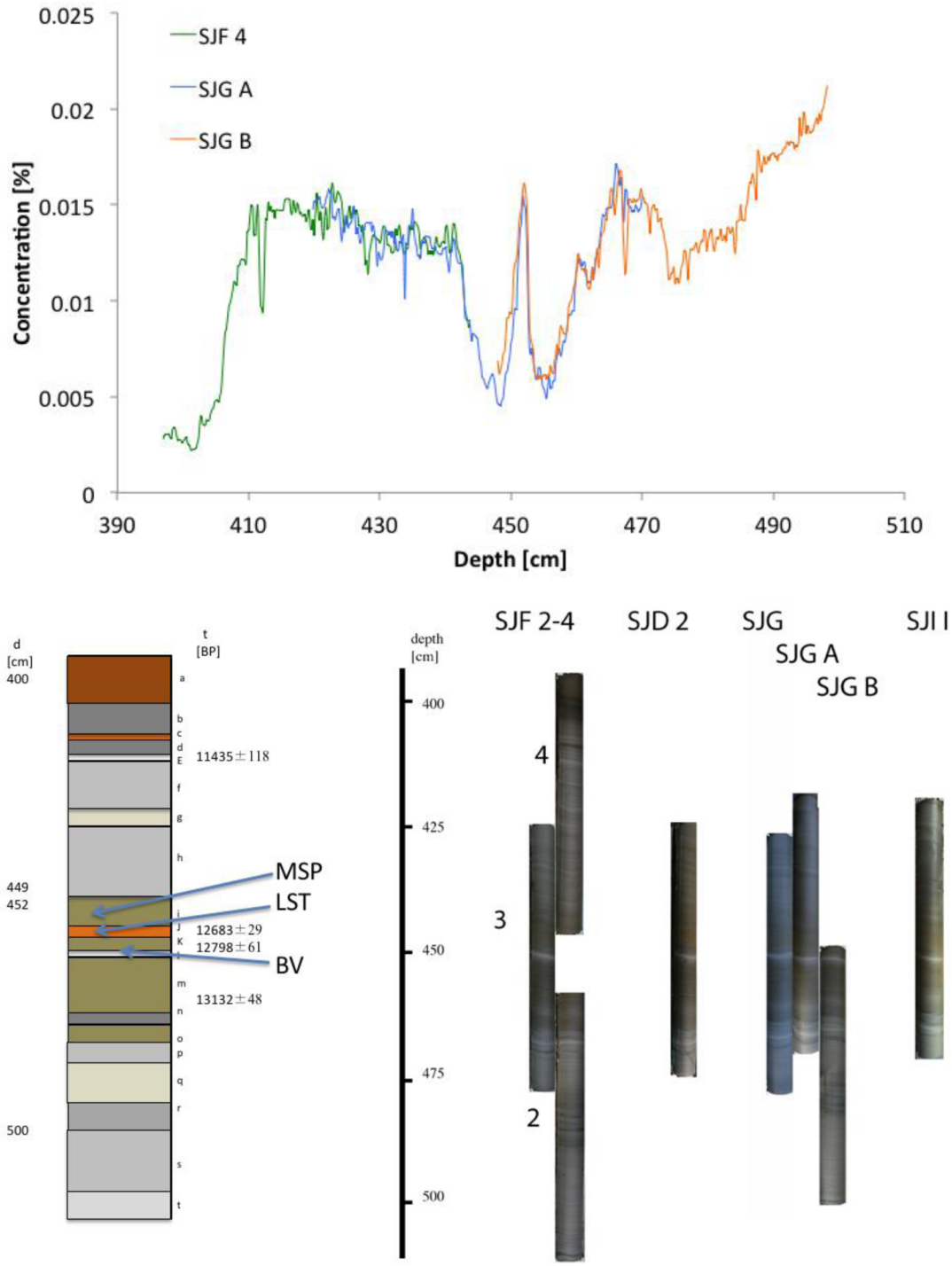

Figure A1. *Top*, Variations in Rb concentration at 2-mm resolution in three ~50-cm-long cores (SJF 4, SJG A, and SJG B) were used to tie them together on a single scale. *Bottom*, stratigraphy of lacustrine sediments (cores SJF 2, SJF 3, SJF 4, SJD 2, SJG, SJG A, SJG B, and SJI I), showing different lithological units (both photos and stratigraphy columns). Changes in deposition reflect lake-level fluctuation and/or sediment input into basin. a = gyttja with clay and silt; b = dark gyttja; c = gyttja with clay and silt; d = black gyttja with clay, silt, and sand; e = white inorganic silt; f = stratified clay with thin (1–3-mm) alteration of silt; g = transition to thicker silt

Core Sediment Composition

One core (SJF 4; fig. A1) contained a transition between gray glacial clay and dark silty gyttja, associated with soil formation and stabilization in the watershed at the Holocene onset that took about 350 y to develop at SJ (Kopáček et al. 2006, 2007). This is because, in SJ, we have a youngest date of 11,475 ± 122 cal BP and the dark material indicating soil formation is ~6 cm above. The accumulation rate from the two youngest dates is 36.4 y/cm (table 3). This indicates that soil formed in less than ~400 y, given that the Holocene started at 11,650 ± 99 cal BP (~5 cm below; Rasmussen et al. 2014). Then, in 11 cm (~400 y) soil formation shows up in the SJ site. Five cores (SJF 3, SJD 2, SJG, SJG A, and SJI I) contained YD sediment that graded downward into brown sediment of Allerød age and then into grayish sediments, probably of Bølling and/or Older Dryas age, that were highly saturated with water. All of these five cores, with the addition of the SJG B core, contained a bright layer in the middle of organic-rich sediment of Allerød age (fig. 1*B*). The deepest core (SJF 2) was taken from near the bottom of the lake sediment sequence.

From the time of lake origin, the sedimentary sequence contains fine to thick interlayers of silt and sand with little organic material (500–470 cm; LOI 4%–6%), followed by organic-rich sedimentation of greenish-brown lake sediment (470–440 cm; LOI up to 13%). These organic-rich sediments are overlain by organic-poor gray silt interlayered with clay (440–400 cm) and, in turn, by organic-rich brown sediments (<400 cm). Each of the 50-cm-long cores was collected from the lake bed approximately 50 cm apart within a 1 × 3-m area. For intercore correlation, we used measurements of Rb to reconstruct an overall geochemical stratigraphy for this site (fig. A1).

Several cores (e.g., SJD 2) contained a bright layer with varve characteristics ("bright varve," or BV; coarse to fine particle gradation). The core material (SJD 2) was sampled to obtain a radiocarbon date from the level just above the BV (fig. A2). Results from Beta Analytic, along with those at three more depth levels, established a chronological model of this material. We used Bayesian statistical analysis (OxCal, ver. 4.2.4) from radiocarbon ages to develop an age-depth model from SJ sediment samples (Bronk Ramsey 2009; fig. A3). The depth of 450.4 ± 1.0 cm, above the BV, gave an age of 12,798 ± 55 cal BP (fig. A2; table 3). The youngest sample, from a depth of 414.3 ± 1.0 cm, provided a modeled date of 11,435 ± 160 cal BP (table 3). Another sample was obtained from a depth of 448.5 ± 1.0 cm, with a modeled age of 12,683 ± 27 BP (table 3). The oldest modeled age was from a depth of 459.2 ± 1.0 cm, 13,132 ± 44 cal BP. However, given that onset of the LST marker horizon was identified in this sediment (12,880 cal BP), we identified that the Bayesian analysis was off by 167 y (table 3).

alteration (2–5 mm); h = stratified clay with thicker silt alteration (3–6 mm); i = grayish-brown gyttja with sand grains and microspherules (MSP); j = green-yellow-red lake gyttja with Laacher See tephra (LST); k = grayish-brown, greasy gyttja with sand grains and organics; l = ash-gray silt of LS age (bright varve [BV]); m = grayish-brown gyttja with sand grains and organics; n = grayish gyttja with sand grains and organics; o = grayish-brown gyttja with sand grains and organics; p = interbedded (3–7-mm) silt and sand; q = gray-greenish, thinly interbedded (2–3-mm) silt and sand; r = interbedded (3–8-mm) dark gray silt; s = thinly interbedded (2–3-mm) silt and sand; t = liquified interbedded (2–5-mm) clay and silt. Age data (cal BP) correspond to Beta Analytic samples 423384, 373184, 366540, and 425248.

Figure A2. Sampling core SJD 2 (see fig. 1*B*) immediately above the bright layer, later identified as the Gerzensee cold oscillation (~13,000 cal BP; Ammann et al. 2013).

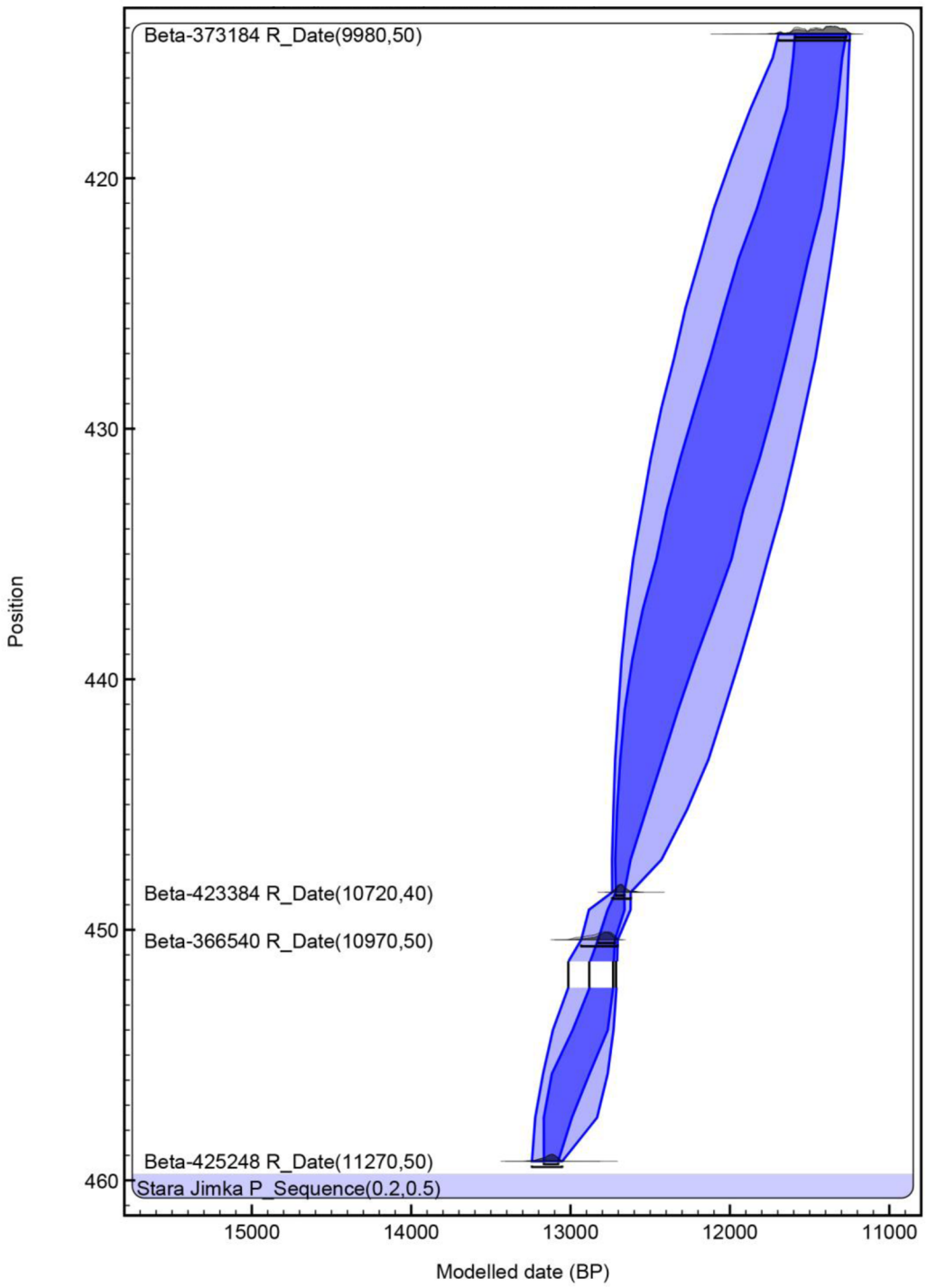

Figure A3. Age model (cal BP) based on four dates from Beta Analytic, all calibrated in OxCal, version 4.2.4, with the IntCal13 atmospheric curve (Reimer et al. 2013). Position indicates sediment depth in centimeters. The white segment of nearly constant age is a sediment portion that accumulated within one season ("bright varve") in the midst of the Gerzensee oscillation (Ammann et al. 2013).

Paleoenvironmental Changes at the YD Cooling Onset

The LS explosion may have influenced the climate before the onset of the YD in central Europe. According to the age-depth model (fig. A3), the LST accumulation started at 12,713 ± 44 cal BP at a depth of 449.0 cm, followed by an MSP-rich layer in the 445.9–446.4-cm depth interval (12,590 ± 82 cal BP). Since the LST age is 12,880 ± 20 cal BP by varve dating, we use this offset to correct our ^{14}C chronology for systematic error of 167 y (table 2).

Both events could be noticeable in the biostratigraphic record. We used several bioindicators, including chironomids (Diptera: Chironomidae), cladocerans (Crustacea: Cladocera), and freshwater macrophytes and algae (figs. 5, A5), to study possible effects on the lake ecosystem. The results indicate a major change in these groups at a core depth of ~446 cm that is considered to represent the onset of the YD cooling episode. However, this change was influenced by a previous significant change in the depth corresponding to the deposition of LST, when the lake assemblages responded to the input of phosphorus and increased lake acidity (fig. 5).

The depth interval immediately following the older edge of the tephra horizon (LST onset) was marked by a high chironomid abundance (289 head capsules per gram of dry sediment) of cold-climate taxa (*Heterotrissocladius grimshawi*–type, *Micropsectra insignilobus/contracta*–type, *Psectrocladius sordidellus*–type, and *Tanytarsus lugens*–type), but without *Micropsectra radialis*–type, a typical indicator of ultraoligotrophic conditions and very cold climate (fig. A5*B*), the most dominant taxon in other parts of Late Glacial sediment sequence from the SJ site (from lake establishment to the depth of ~470 cm and later during the peak of YD cooling; D. Vondrák, unpublished data). The interval immediately following the YDB layer (onset of the YD) exhibits a distinct shift in the relative abundance of several chironomid taxa, including an increase in *Chironomus athracinus* type and the first occurrence of *M. radialis* type. We found synchronous changes in cladocerans at the YDB layer (~446 cm). This transition is characterized by both a temporary increase in total cladoceran abundance and a decrease in relative abundance of planktonic species (genera *Bosmina* and *Daphnia*; fig. A5*C*).

Between the LS event and the YDB layer containing MSPs, nine species of Cladocera occurred in the lake; after the onset of YD, however, only three previously dominant species (*Acroperus harpae*, *Alona affinis*, and *Bosmina longispina*) remained. These species are known to be able to withstand the water shortage of ~40 d presumed for the SJ paleolake. We hypothesize that the decline in planktonic species is a consequence of a hydrological change and/or less convenient lake water chemistry.

Pollen sequences from the SJ site (core SJD 2) revealed that at the time of the tephra deposition, the pollen assemblages decreased in birch (*Betula nana*) and increased in pine (*Pinus*) and tundra-type heliophytes, reflecting temporary cooling. At the time of the YDB layer, further abrupt changes occurred in pollen assemblages. While the ratio of tree (arboreal) pollen to other (nonarboreal) pollen decreased during the tephra deposition, it increased across the YDB (MSP) layer. Across the YDB layer pine pollen suddenly decreased, while birch pollen increased (fig. A5*A*). This behavior is consistent with the disturbance of the ecosystem (de Klerk et al. 2008).

We continuously measured charcoal abundances and limited our analyses to particles >125 μm that are typically produced by local fires, because long-distance dispersion is restricted for particles of that size class and larger (fig. A5*A*). Three intervals are marked by distinct increases in charcoal. The first interval is 11 cm of high charcoal concentrations just below the LST (463–452 cm). This is followed by a 3-cm interval with low charcoal concentrations (452–449 cm) and 8 cm of high concentrations within and above the YDB layer (449–441 cm).

The high-resolution climate record suggests that YD cooling occurred in Europe approximately 200 y after the LS event (Brauer et al. 1999; Wulf et al. 2013). The correlation between the YDB layer in the SJ site and an abrupt shift in climate is consistent with the YD impact hypothesis describing a transient event that triggered the onset of the YD cooling episode (Firestone et al. 2007).

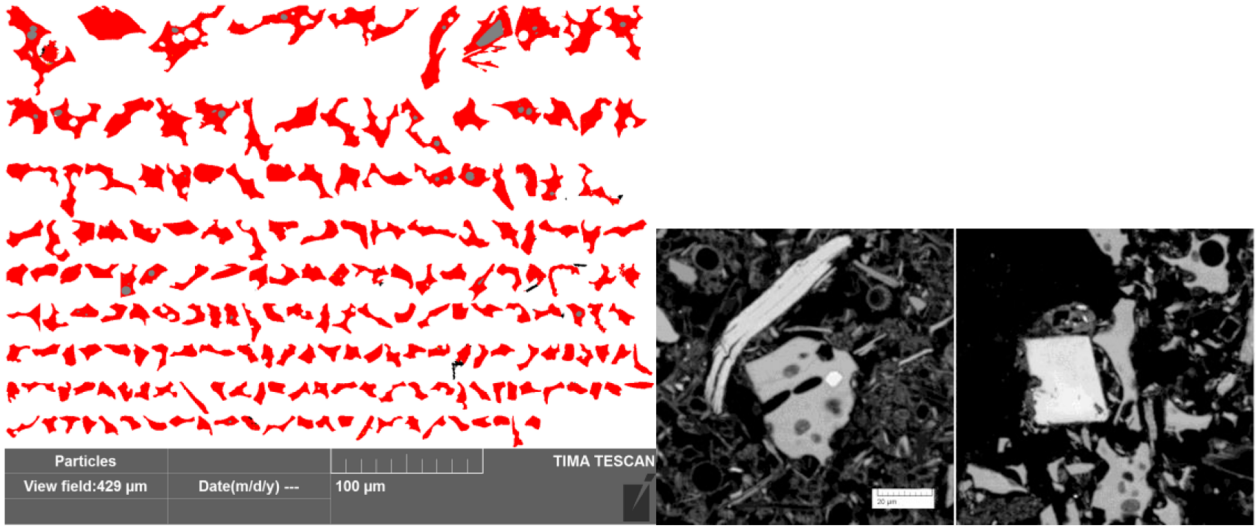

Figure A4. Examples of glass fragments. *A*, Results of a computerized process used to detect glass shards, detected with a scanning electron microscope, contained within the Stara Jimka sediment at a depth of 449.2 cm (fig. 4; table 3); TIMA = TESCAN integrated mineral analyzer. *B*, Glass fragment containing a clinopyroxene (CPX; =augite) inclusion. *C*, CPX crystal located outside the glass fragments.

Appendix from G. Kletetschka et al., Cosmic-Impact Event in Lake Sediments from Central Europe Postdates the Laacher See Eruption and Marks Onset of the Younger Dryas

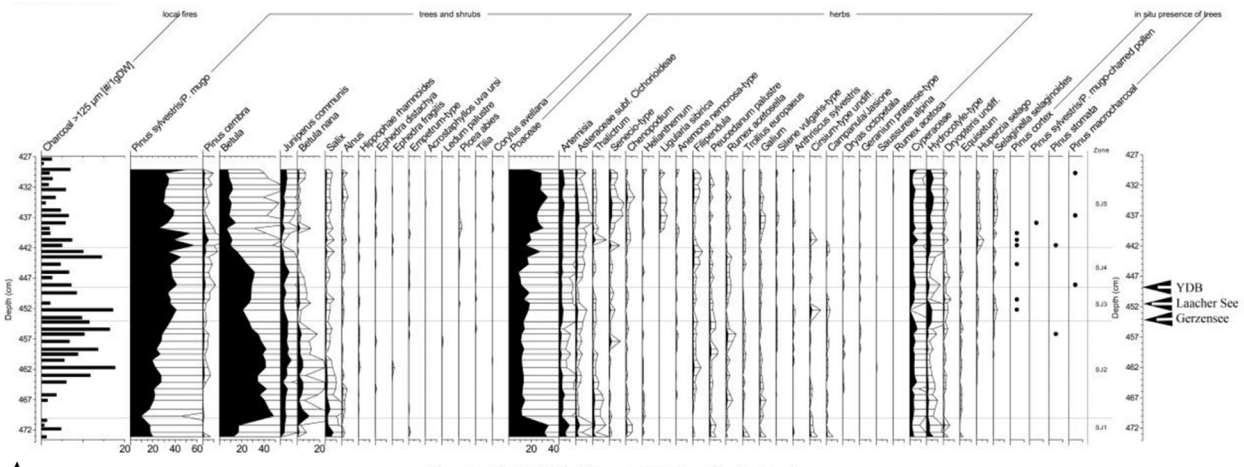

BV Morphology

The bright layer (BV) used for correlating the cores in addition to Rb content has an interesting morphological characteristic suggesting a rapid accumulation during one season (fig. A6). It is coarse grained at the base (50 μm) and fine grained (<5 μm) toward the top.

A TIMA was used in automatic dot-mapping mode (see "SEM" above) to obtain the distribution of the fine fragments of glass composition. A 1-mm-wide and 5-cm-long section through a sedimentation profile was scanned with more than 549 million data points, at which were performed 12 million EDS analyses to provide the base for localization and distribution analysis of glass fragments. The composition used in this case is listed in table A2.

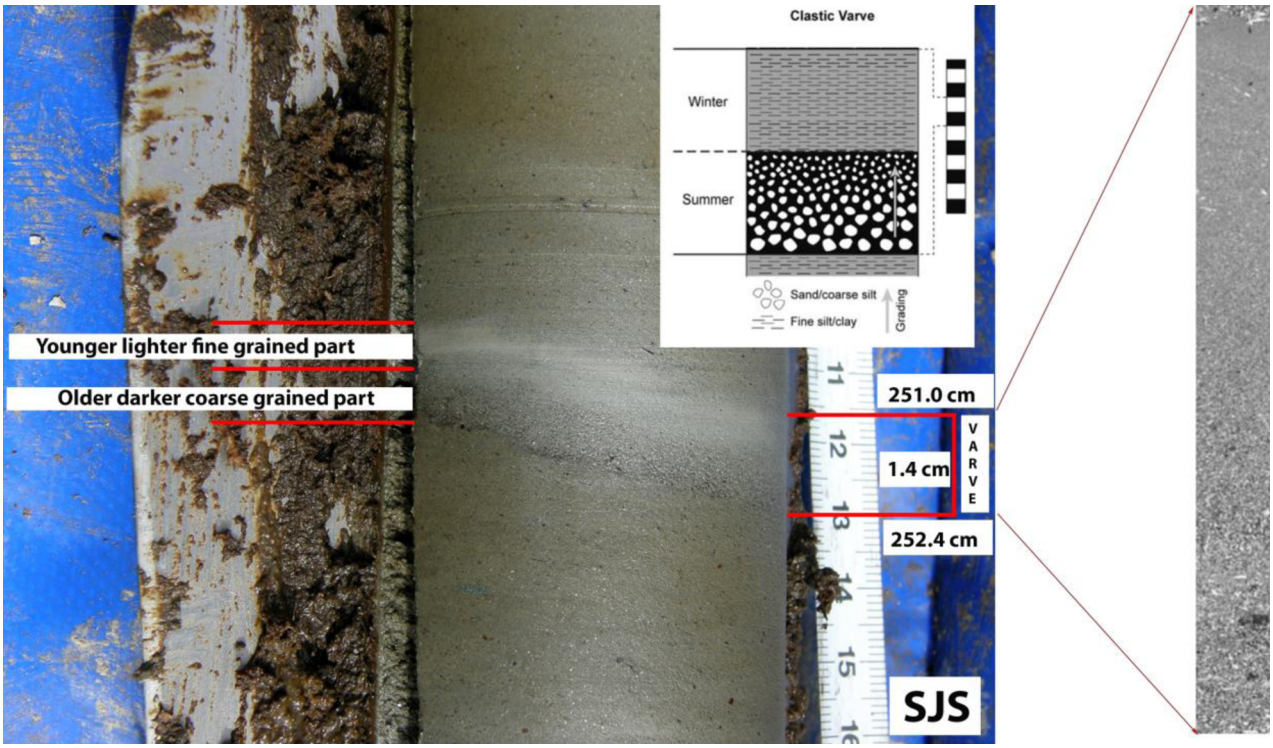

Figure A6. Images of the bright-varve layer (BV) within the Stara Jimka sediment (SJS; core SJI I). *Left*, photograph of the BV immediately after core extraction. *Right*, scanning electron microscope image corresponding to the photo. Sediment grades from coarse to fine from the lower part to the upper part of the core. The inset shows the general varve morphology cartoon (Lowe and Walker 2015).

Figure A5. *A*, Number of charcoal particles (>125 μm) and pollen in sediment samples continuously taken at increments across the microspherule (MSP; = Younger Dryas boundary [YDB]) layer that is just above the Laacher See tephra (LST) deposit. The Gerzensee cold event (GO) is marked just below this deposit. *B*, Relative abundances of the dominant (>4 %) chironomid taxa in 12 selected 2-mm-thick layers of core SJF 3, shown as percentages relative to the total number of chironomid head capsules per sample. Taxa are arranged with respect to their optimum temperature in the Swiss Alps modern calibration data set (Heiri et al. 2011); taxa with coolest optimum temperatures are shown on the left and taxa with the warmest optimum temperatures on the right. Taxa not present in the data set are arranged in alphabetical order. *Paracladius* sp. and *Micropsectra radialis*–type were rare morphotypes, but they are included as important cold-climate indicators. Positions of the GO, LST, and YDB (MSP) layers are indicated by gray bars across the diagram. *C*, Abundances and the total number of Cladocera remains in nine selected 2-mm-thick layers of the SJF 3 core between 441 and 453 cm. The data are based on chitinous remains of shells, head shields, postabdomens, or ephippia (one type of remains being representative for each taxon). For ephippia presence/absence, three additional layers were analyzed. The taxa are divided into typically pelagic (genera *Daphnia* and *Bosmina*) and preferably littoral (family Chydoridae) and arranged alphabetically in each group. Positions of the GO, LST, and YDB (MSP) layers are indicated by gray bars across the diagram.

Table A1. Nb, P, S, and C Concentrations Measured by Destructive Methods, Including ICP-MS, for SJG-B Sediment Layers Containing Laacher See Tephra (LST)

Sample	Depth (cm)	Dry mass/vol (g/mL)	Nb (mg/kg)	P (mg/kg)	S (%)	C (%)	Notes
01–1	467.7	.1/50	17.2	336	.02	.29	Sister sample to 01–2
01–2	467.7	.1/50	17.7	270	.03	.33	Sister sample to 01–1
02–T	467.2	.1/50	17.5	314	.02	.35	"Older varve" dark part; no space between 02–S and 02–T
02–S	466.7	.1/50	18.1	422	.03	.38	"Older varve" light part; no space between 02–S and 02–T
03–1	453.2	.05/25	18.2	309	.1	4.62	Sister sample to 03–2; both mixed for Nb
03–2	453.2	.05/25	18.2	309	.12	4.73	Sister sample to 03–1; both mixed for Nb
04–T	**452.5**	**.05/25**	**18.4**	**301**	**.05**	**2.77**	**"BV" dark part; no space between 04–S and 04–T**
04–S	**451.8**	**.1/50**	**20.8**	**341**	**.04**	**1.1**	**"BV" light part; no space between 04–S and 04–T**
05–1	449.9	.05/25	19.3	688	.11	4.21	Sister sample to 05–2
05–2	449.9	.05/25	18.3	499	.12	4.06	Sister sample to 05–1
06–1	**449.0**	**.05/25**	**32.2**	**1825**	**.12**	**4.41**	**With glass, sister sample to 06–2; mixed for Nb**
06–2	**449.0**	**.05/25**	**32.2**	**1825**	**.12**	**4.41**	**With glass, sister sample to 06–1; mixed for Nb**
07–1	**447.9**	**.05/25**	**35.8**	**2152**	**.15**	**4.96**	**With glass, sister sample to 07–2**
07–2	**447.9**	**.05/25**	**44.7**	**2416**	**.14**	**4.92**	**With glass, sister sample to 07–1**
08–1	446.7	.05/25	18.7	991	.1	4.23	Sister sample to 08–2; mixed for Nb
08–2	446.7	.05/25	18.7	991	.1	4.23	Sister sample to 08–1; mixed for Nb

Note. Boldface indicates layers containing LST. BV = bright varve.

Table A2. Laacher See Tephra (LST)–Like Composition Used to Identify the Glass Fragments via Electron Diffraction Scattering with Automated Dot-Mapping Analysis of the Sedimentary Profile (Core SJI I)

	O	F	Na	Mg	Al	Si	P	Cl	K	Ca	Ti	Mn	Fe
Glass 1, weight normalized:													
Avg. concentration (%)	50.83	1.51	6.14	.36	10.34	23.25	.19	.32	3.80	.51	1.56	.06	1.08
SD (%)	1.83	.24	.53	.03	.40	1.34	.01	.04	.40	.09	.07	.04	.23
Glass 2, weight normalized:													
Avg. concentration (%)	49.62	1.11	3.57	.52	10.46	26.51	.22	.11	4.57	.77	1.72	...	.76
SD (%)	1.95	.31	1.24	.30	.84	1.46	.06	.07	1.86	.55	.25	...	.81
Glass 3, weight normalized:													
Avg. concentration (%)	50.54	.94	4.63	.36	10.98	27.63	.19	.06	3.83	.50	.00	.00	.30
SD (%)	1.37	.08	.71	.10	.81	1.04	.03	.03	1.38	.45	.00	.00	.26
Feldspar QQQ, weight normalized:													
Avg. concentration (%)	50.47	.85	6.11	.29	12.10	27.40	.20	.02	.35	2.12	.00	.00	.04
SD (%)	1.08	.06	.51	.02	.58	.97	.04	.01	.10	.95	.00	.00	.08

Note. See "SEM." Glass 1 composition was correlated with the large fragments that include gas textures and their distribution (figs. 4*A*, A4, A7). Forty large fragments were used for microprobe analysis (table 2). Glasses 2 and 3 were also detected but contained less iron than LST. Avg. = average; QQQ = quartz-quartz-quartz.

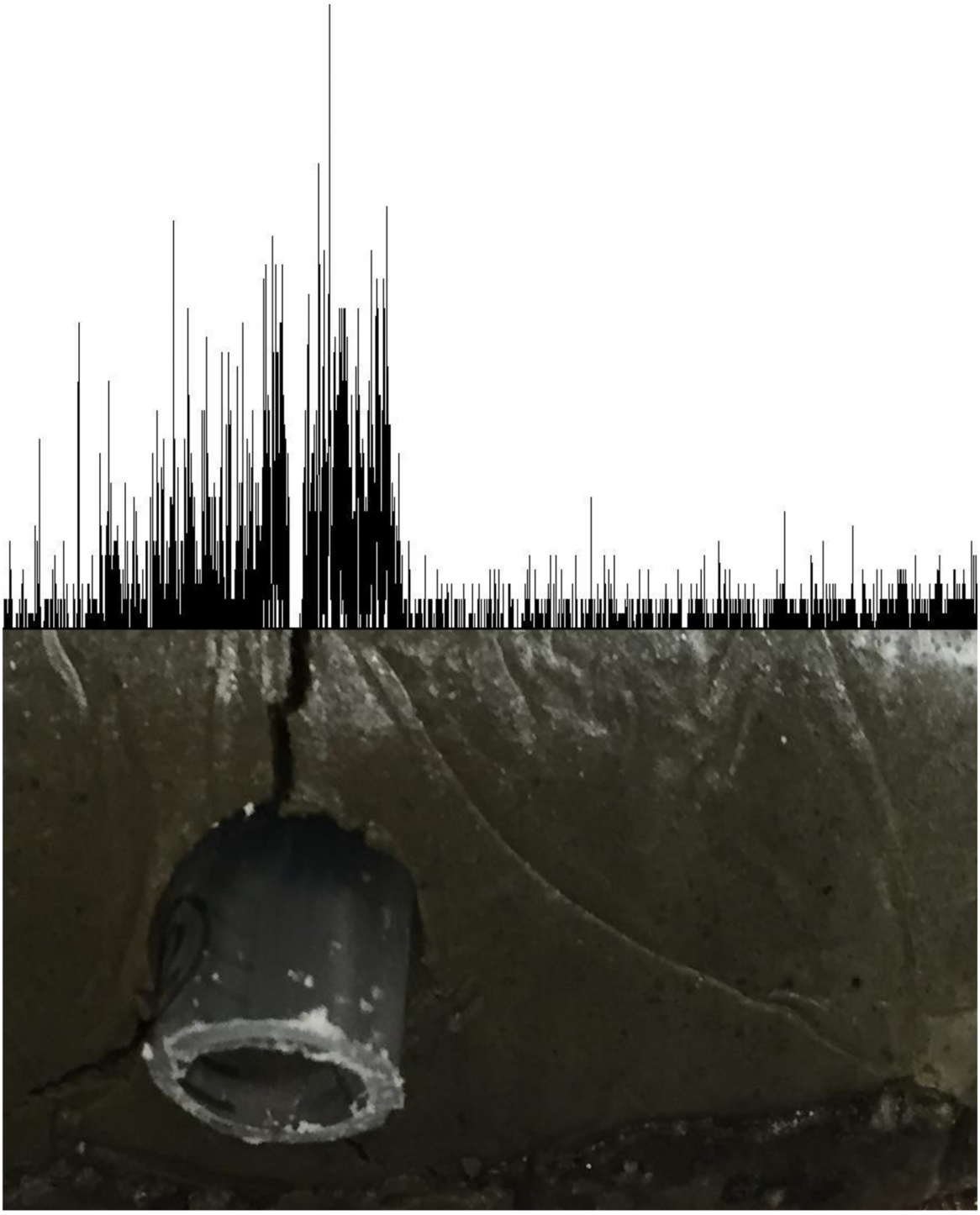

Figure A7. Scanning electron microscopy identification of the signal of the relative amount of volcanic glass fragments along the ~4-cm-long sedimentary profile. The plastic cylinder (10 mm in outside diameter) in the core photograph shows the location of the sampling for the ^{14}C date (Beta Analytic ID 423384, age: 12,683 ± 27 cal BP). The core depth increases toward the right side of the image.

Three Stages of the YD Onset

Changes in the weathering index Th/K across the onset of the YD after the glass deposition, along with the MSPs, allow identification of three distinct intervals (fig. 3*E*) The earliest starts at a depth of 448.3 cm, and it is interrupted by the horizon containing MSPs (~446.4–445.8 cm). This interval represents an oligomesotrophic lake stage with abundant aquatic organisms (dominance of cladocerans [*Acropenus harpae*, *Alona affinis*, *Eurycercus lamellatus*, *Bosmina longispina*, and *Daphnia longispina* gr.] and chironomids [*Tanytarsus lugens*–type, *Psectrocladius sordidellus*–type, and *Micropsectra insignilobus/contracta*–type]) and the presence of indicators of temperate climatic conditions such as *Ablabesmyia* and *Tanytarsus pallidicornis*–type 2, all supported by the high phosphorus input from the precedent LST event (figs. 5*D*, 5*F*, A5*B*, A5*C*).

The second stage covers the depth interval ~446.1–442.9 cm. It is characterized by a gradual decrease in both cladoceran and chironomid abundance, a reduction of planktonic taxa (viz., *D. longispina* gr.), and a rise in cold stenothermic taxa (*Corynoneura arctica*–type, *M. insignilobus*/*contracta*–type; first appearance of *Paracladius* and *Micropsectra radialis*–type). These changes show a distinct harshness of environmental conditions (a decrease in water air/water temperature and lake trophy status). Moreover, lake-water acidity may have plunged below pH 5, as indicated by the appearance of *Alonopsis elongata* and the sudden decrease of *T. lugens* and *D. longispina* gr. (figs. 5*D*, 5*F*, A5*B*, A5*C*). The temporal increase in *Chironomus anthracinus*–type (figs. 5*F*, A5*B*) we interpret as a result of possible decrease in oxygen concentration near the bottom and/or an increase in the muddy portion of the substrate in the lake basin. The third stage of the Th/K decrease starts at a depth of 442.9 cm. Here, the abundance of chironomid and cladoceran remains, as well as the number of documented taxa, is very low. *Daphnia longispina* gr. and chironomid indicators of temperate climatic conditions (*Ablabesmyia*, *T. pallidicornis*–type 2) are missing, and cold stenothermic taxa dominate (*Heterotrissocladius grimshawi*–type, *M. insignilobus*/*contracta*–type, *M. radialis*–type, and *T. lugens*–type).

MSP-Rich Layer (YDB)

An extraterrestrial impact is a transient event that produces a turbulent impact plume and/or a fireball cloud of extremely high temperatures (Bunch et al. 2012). Clouds of this kind contain vapor, shock debris, breccia, melted rock fragments, and MSPs derived from either target or impactor materials. To investigate whether such material is present at SJ, we used a standard technique (Israde-Alcántara et al. 2012) to separate the magnetic fraction from samples of core sediment. Using an optical microscope, we found no detectable MSPs in SJ sediments below the LST horizon down to the 470-cm depth. They suddenly appear in a 0.5-cm interval of lake sediment above the top of the LST layer, in a thin layer from ~445.9 to 446.4 cm below the ground surface.

The high-temperature quenched glassy MSPs were observed at a remarkably high concentration of 17,000/kg. Concentrations are lower at deeper levels and continuously increase upward, peaking at 446.0 cm. Bioturbation and/or gravitational settling, with the MSPs moving downward to deeper levels, best explains this variable vertical distribution (fig. A8). In addition, we observed more Fe-rich MSPs toward the bottom of the MSP layer. This distribution is consistent with the atmospheric settling of MSPs from sudden formation within the dust cloud, where lightning discharge is capable of melting the dust material (Shevtsov et al. 2016). For this process we found evidence in the magnetism of one spherule that exceeded the normal level of magnetization within the geomagnetic field (fig. A10; Wasilewski and Kletetschka 1999).

Overlapping the group of glassy MSPs, we observed a narrower peak in a second type of spherulitic object: nonglassy, unmelted pyritic framboids, with diameters similar to those of the MSPs. Framboids peak at 4000/kg at a depth of 445.0–445.6 cm (fig. 3). The two types of spherules exhibit distinct but closely overlapping peaks in abundance (fig. 3). Both framboids and quenched MSPs disappear from the record above 445 cm below ground.

The MSPs range from 10 to 40 μm in diameter and typically display highly reflective surfaces. Some show evidence of melting, displaying either tear-like droplets on their surfaces and/or aerodynamic teardrop shapes (fig. 2). Observations with an SEM revealed that the outer surfaces of MSPs have either crystalline dendritic patterns (fig. 4*D*) or polygonal (soccer-ball) textures (fig. A9).

These crystalline textures are characteristic of high-temperature melting followed by abrupt quenching, thus eliminating biogenic, detrital, or diagenetic origins (Bunch et al. 2012; Wittke et al. 2013). Similar MSPs reported from the YDB layer are proposed to be due to high-temperature ablation and/or the melting of terrestrial rocks as ejecta (Firestone et al. 2007). Analyses by SEM-EDS shows that some SJ MSPs contain melted siliceous glass (lechatelierite), representing

evidence of high-temperature melting (Bunch et al. 2012). Such glass forms within the impact plume at temperatures ranging from 1720°C, the melting point of quartz, to >2230°C, its boiling point.

Because lechatelierite can form in fulgurites during high-temperature lightning strikes (Wasilewski and Kletetschka 1999), we conducted tests to determine whether lightning could have formed the MSPs at SJ. Lightning-melted spherules quench to low temperatures in a fraction of a second, making some of them capable of retaining the magnetic field generated by lightning, which decays more slowly than the material can quench (Wasilewski and Kletetschka 1999). Thus, lightning-produced glass (fulgurites) preserves magnetization near saturation (Wasilewski 1981; Wasilewski and Kletetschka 1999), identified as lightning remanent magnetization (LRM).

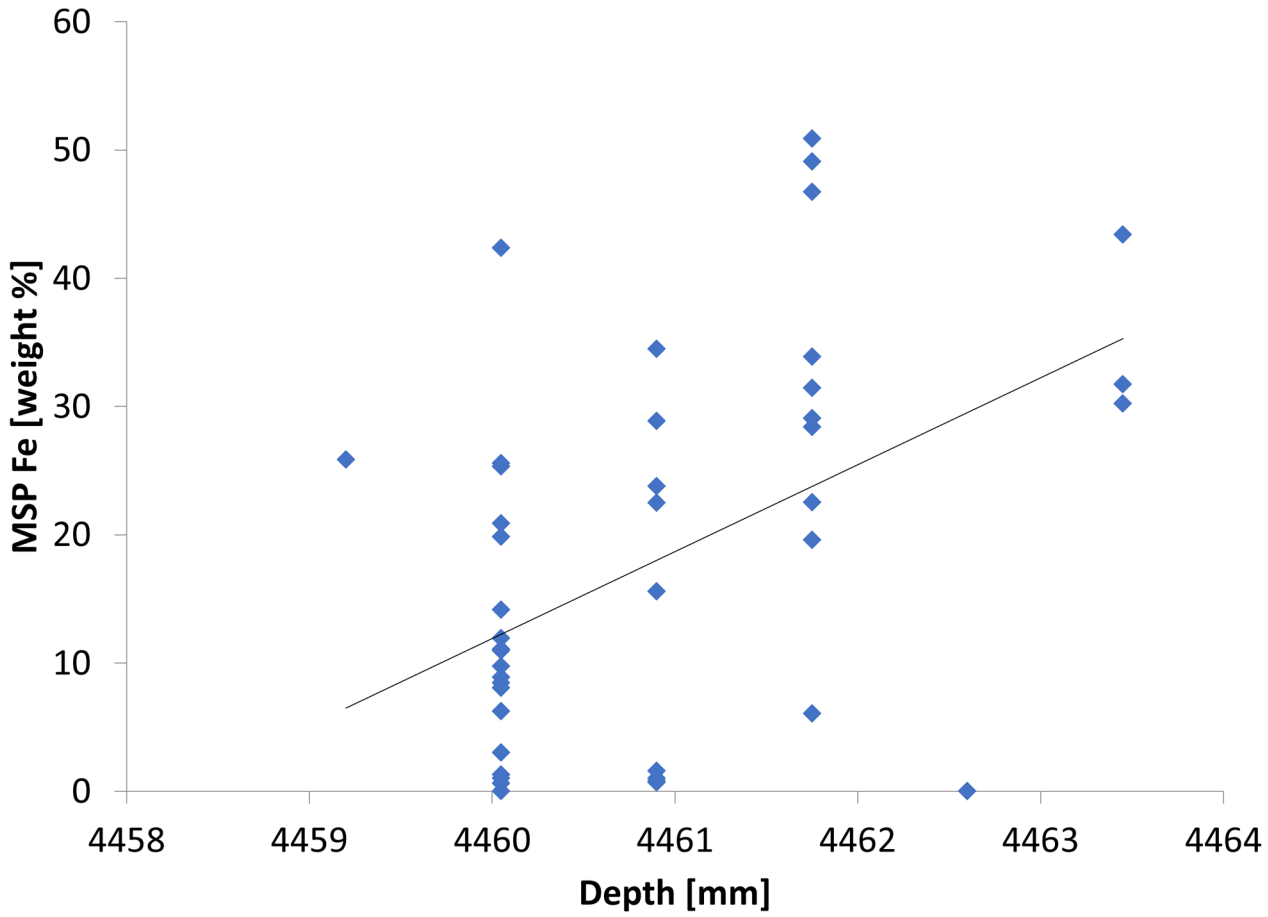

Figure A8. Weight percent of Fe in individual spherules from a vertical suite of samples over the microspherule (MSP) layer at Stara Jimka. The spherule assemblages exhibit a general trend of increasing Fe with greater depth.

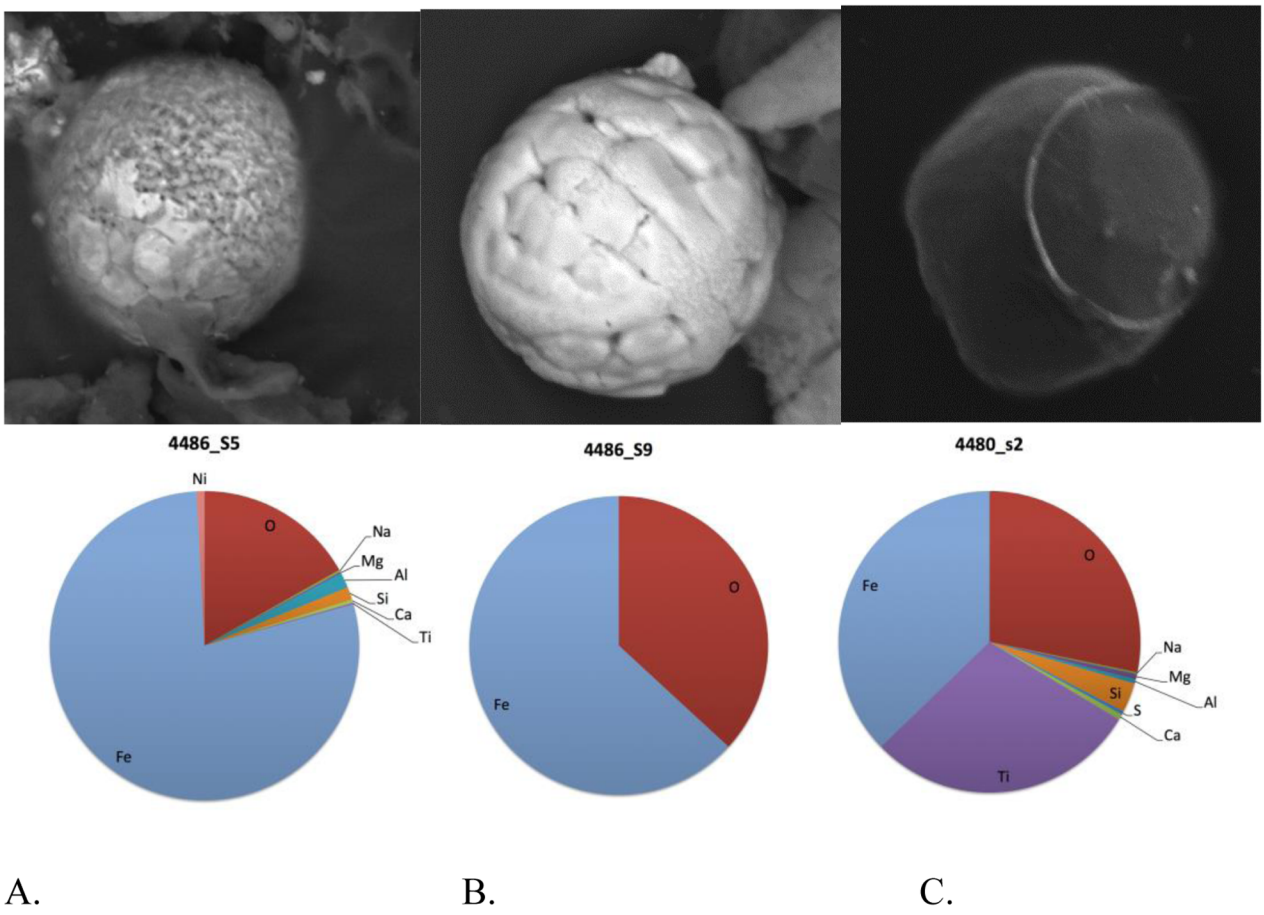

Figure A9. Scanning electron microscopy images of Fe-rich microspherules (MSPs; 20 μm in diameter). *A*, MSP containing a small amount of nickel. *B*, MSP with soccer-ball-like texture; *C*, MSP with deformation ring formed during collision while quenching. Elemental composition of these spherules is shown below the images.

LMR Analysis

We extracted MSPs from the bulk sediment by using nonmagnetic tools (see "MSP Extraction"). Our analysis revealed that magnetization levels are approximately an order of magnitude lower than magnetization in the saturated state (fig. A10). Demagnetization of this state revealed high-coercivity material, and the MSPs exhibit thermoremanent magnetization acquired when cooled in the presence of a field stronger than the geomagnetic field (Kletetschka et al. 2006). The results for one of two SJ MSPs are consistent with production by lightning discharge in the tephra cloud.

The MSP layer contains a variety of spherules with different compositions. The most abundant group appears glassy and is of rhyolitic, tephritic, dacitic, or andesitic composition. Others are composed mostly of oxides of silica and iron, consistent with melting of target rocks and/or condensation from silicon-iron vapor in the fireball (fig. 2); still others are melted Fe-rich magnetite, with almost no other elemental abundance. Another group has a Ni-Fe composition (figs. 2, A9), derived either from the impacting body or from Ni-rich target rocks. Carbon spherules and Si-rich MSPs are also present but less abundant. An earlier study suggested that all previously identified YDB MSPs are simply detrital grains or framboidal spherules (Haynes et al. 2010), but we refute that claim by demonstrating that abundant MSPs exhibit quench-melted textures, readily observed with SEM. In addition, some of them are magnetized to more intense levels, indicating that they were magnetized by the magnetic field of lightning (Wasilewski and Kletetschka 1999). Others show no remanent magnetism, indicating that they were not formed by lightning.

Along with glassy spherules (fig. 2), we observed iron-rich MSPs with quenched textures (fig. A9*A*, A9*B*). One unusual spherule exhibited a ring on one side (fig. A9*C*), possibly due to collision between particles, similar to those found at other YDB sites (Wittke et al. 2013). These MSPs are dominantly of iron composition, with Ca, Si, and Al. The spherule with the ring is composed of Ti, less common among the MSPs at the SJ site.

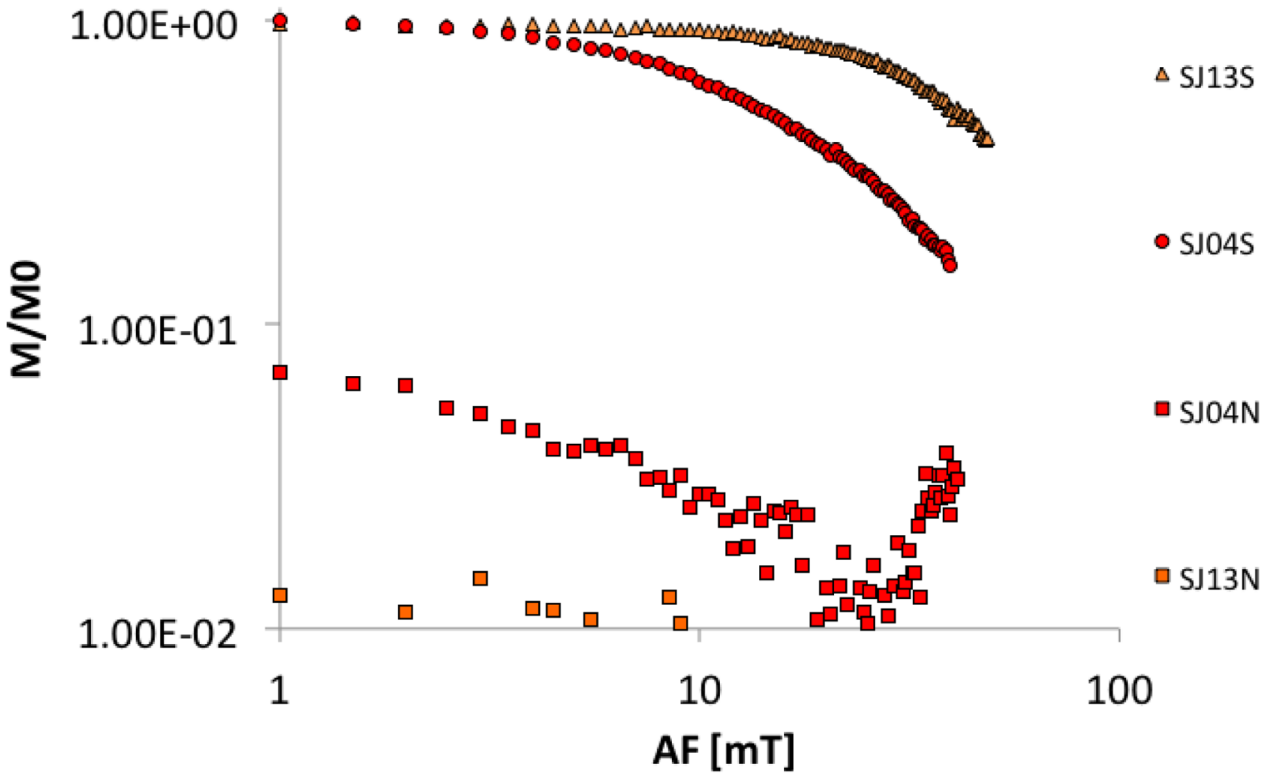

Figure A10. Level of magnetization M normalized by their saturated level M_0 (M/M0) of magnetic spherules from Stara Jimka site. Lower curves indicate level of demagnetization, by stepwise-applied alternating magnetic field of increasing magnitude, of its natural remanent magnetization (SJ04N, SJ13N). Upper curves show level of demagnetization, by stepwise-applied alternating magnetic field of increasing magnitude, of the same spherule after it was magnetically saturated (SJ04S, SJ13S). AF = alternating field.

Geochemical Anomalies at the YDB Layer

We performed XRF analyses along all cores over the interval containing LST and MSPs and identified geochemical anomalies associated with LST in Ca, Nb, and P (figs. 3, A1, A11). The most pronounced is an anomaly in P that we were able to use as a distinct initial marker horizon while scanning the cores. This glass-rich layer is indistinctly seen in optical light (fig. A1). The phosphorus is contributed from glass accumulation containing a measurable amount of phosphorus. The bulk of the phosphorus signal comes from the aerosol grains mixed in the YDB material (fig. 4). The absolute levels of selected elements were measured with induced plasma mass spectrometry at the Charles University and confirmed the relative variation of Ca, Nb, and P (fig. A11; table A1) across the volcanic glass–containing layer (LST).

When we plot the Th/K ratio, a weathering indicator (Taylor et al. 2010), over the time period of the Allerød transition (fig. 3; table 2), we find that the lake sediment had minimum weathering until a depth of 460 cm, when the weathering increased, probably in connection with soil-forming processes in the region. This period was transected by the LS eruption that caused climate change, in which the Th/K indicator sharply decreased as a result of an increase in the rate of sediment deposition. The LOI data tightly follow this trend (figs. 3, 5*A*).

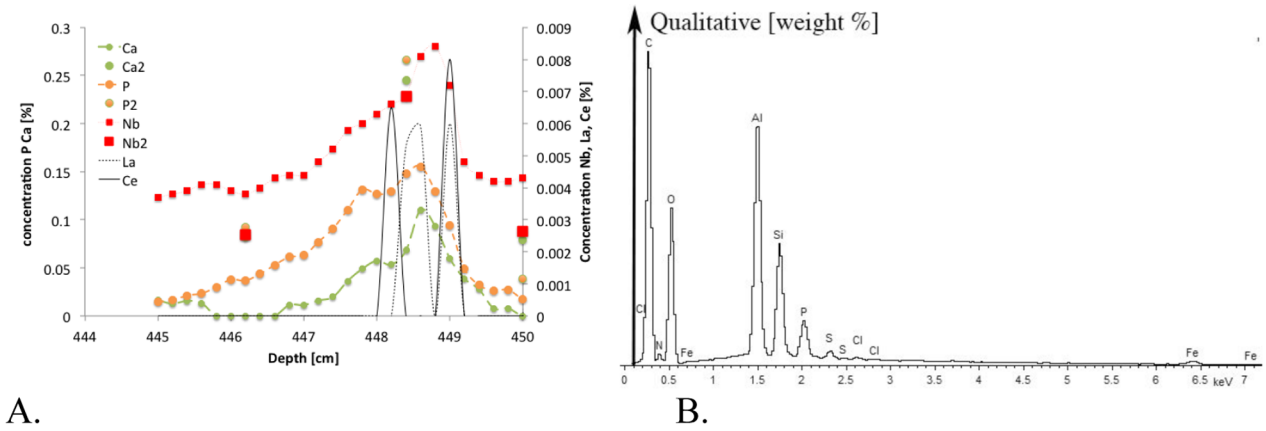

Figure A11. *A*, Anomalies in elemental composition, P, Ca, and Nb. Single points for P2, Ca2, and Nb2 represent ICP-MS measurements of the same material. Lanthanum (La) and cerium (Ce) were detected by X-ray fluorescence above the detection level for the depth associated with Laacher See tephra. *B*, Qualitative spectrum of an aerosol grain incorporated in the tephra glass within a carbon-coated polished thin section shows presence of nitrogen (N), carbon (C), oxygen (O), phosphorus (P), sulfur (S), silicon (Si), aluminum (Al), iron (Fe), and chlorine (Cl).

Magnetic Susceptibility and Iron Content of the Sediment

We analyzed bulk samples for magnetic susceptibility (MS) measurement over the depth of interest. We determined that changes in MS parallel those in Fe concentrations, determined with XRF analysis. Both parameters increased during the deposition of LST (fig. A12). This indicates that the YDB event did not deposit a significantly larger amount of the inorganic material to enter into the lake, while the LST event did.

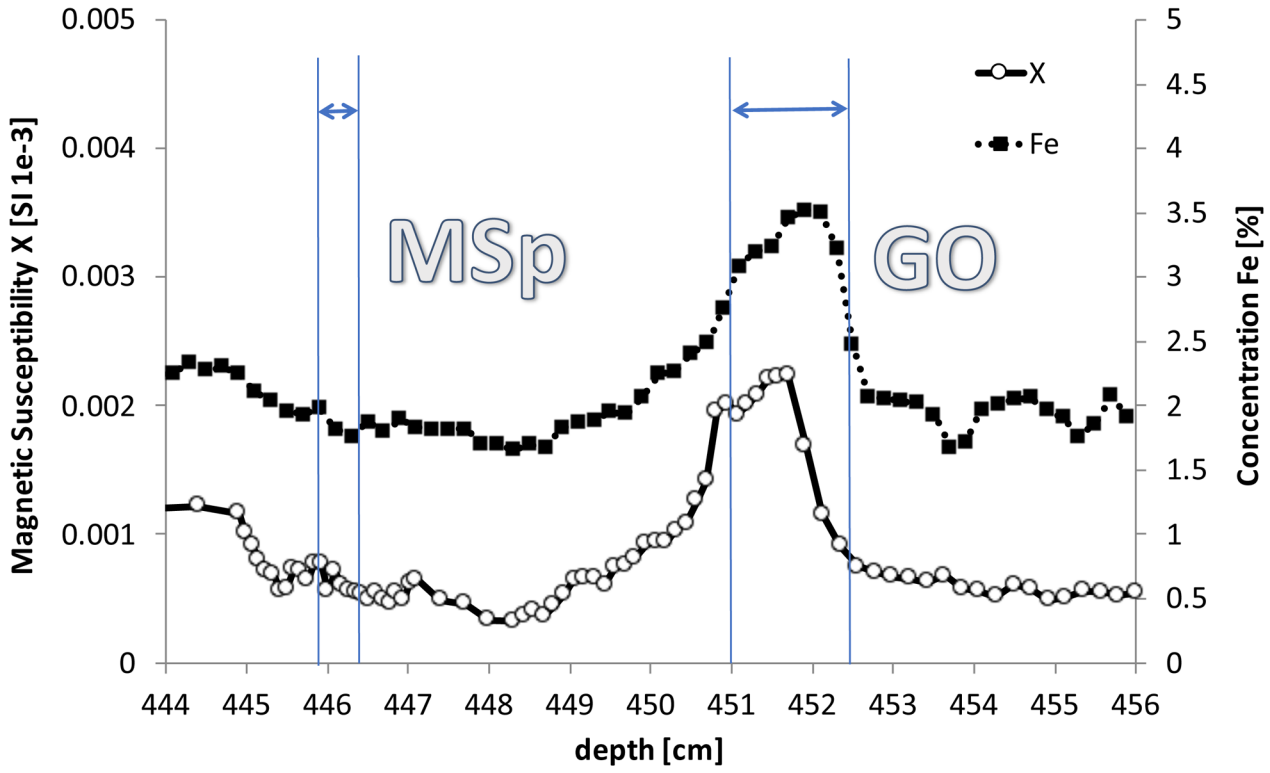

Figure A12. Magnetic susceptibility of wet sediment (left axis) with X-ray fluorescence–measured Fe concentration (right axis). MSp = microspherule (Younger Dryas boundary) layer; GO = Gerzensee oscillation.

Composition of LST Glass Found in SJ Sediment

Table A1 shows the composition of the LST glass collected at the SJ site from two levels. Tephra glass is clearly from the middle LS eruption sequence in the East Eifel Volcanic Field, when its composition is compared to that of known sites containing these tephras (table 3; Wulf et al. 2013). However, the date of the sediment is 167 y younger than the LS event, and we corrected for this systematic offset (table 2).

REFERENCES CITED ONLY IN THE APPENDIX

Brooks, S. J.; Langdon, P. G.; and Heiri, O. 2007. The identification and use of Palaearctic Chironomidae larvae. Tech. Guide no. 10. London, Quaternary Research Association.

Gottlieb, P.; Wilkie, G.; Sutherland, D.; Ho-Tun, E.; Suthers, S.; Perera, K.; Jenkins, B.; Spencer, S.; Butcher, A.; and Rayner, J. 2000. Using quantitative electron microscopy for process mineralogy applications. J. Miner. Met. Mater. Soc. 52(4):24–25.

Haynes, C. V., Jr.; Lauretta, D. S.; and Ballenger, J. A. M. 2010. Reply to Firestone et al.: no confirmation of impact at the lower Younger Dryas boundary at Murray Springs, AZ. Proc. Natl. Acad. Sci. USA 107:E106. doi:10.1073/pnas.1005384107.

Heiri, O.; Brooks, S. J.; Birks, H. J. B.; and Lotter, A. E. 2011. A 274-lake calibration data-set and inference model for chironomid-based summer air temperature reconstruction in Europe. Quat. Sci. Rev. 30:3445–3456. doi:10.1016/j.quascirev.2011.09.006.

Heiri, O.; Brooks, S. J.; Renssen, H.; Bedford, A.; Hazekamp, M.; Ilyashuk, B.; Jeffers, E. S.; et al. 2014. Validation of climate model–inferred regional temperature change for late-glacial Europe. Nat. Commun. 5:4914. doi:10.1038/ncomms5914.

Kletetschka, G.; Fuller, M. D.; Kohout, T.; Wasilewski, P. J.; Herrero-Bervera, E.; Ness, N. F.; and Acuna, M. H. 2006. TRM in low magnetic fields: a minimum field that can be recorded by large multidomain grains. Phys. Earth Planet. Interiors 154:290–298. doi:10.1016/j.pepi.2005.07.005.

Kliment, Z.; Matoušková, M.; Ledvinka, O.; and Královec, V. 2011. Trend analysis of rainfall-runoff regimes in selected headwater areas of the Czech Republic. J. Hydrol. Hydromech. 59:36–50. doi:10.2478/v10098-011-0003-y.

Kopáček, J.; Marešová, M.; Hejzlar, J.; and Norton, S. A. 2007. Natural inactivation of phosphorus by aluminum in preindustrial lake sediments. Limnol. Oceanogr. 52:1147–1155.

Kopáček, J.; Marešová, M.; Norton, S. A.; Porcal, P.; and Veselý, J. 2006. Photochemical source of metals for sediments. Environ. Sci. Technol. 40:4455–4459. doi:10.1021/es0600532.

Lowe, J. J., and Walker, M. J. C. 2015. Reconstructing Quaternary environments (3rd ed.). London, Routledge.

Taylor, G. J.; Martel, L. M. V.; Karunatillake, S.; Gasnault, O.; and Boynton, W. V. 2010. Mapping Mars geochemically. Geology 38:183–186. doi:10.1130/g30470.1.

Wiederholm, T. 1983. Chironomidae of the Holarctic region: keys and diagnoses. Pt. 1. Larvae. (Entomol. Scand. Suppl. vol. 19). Södra Sandby, Entomologica Scandinavica.